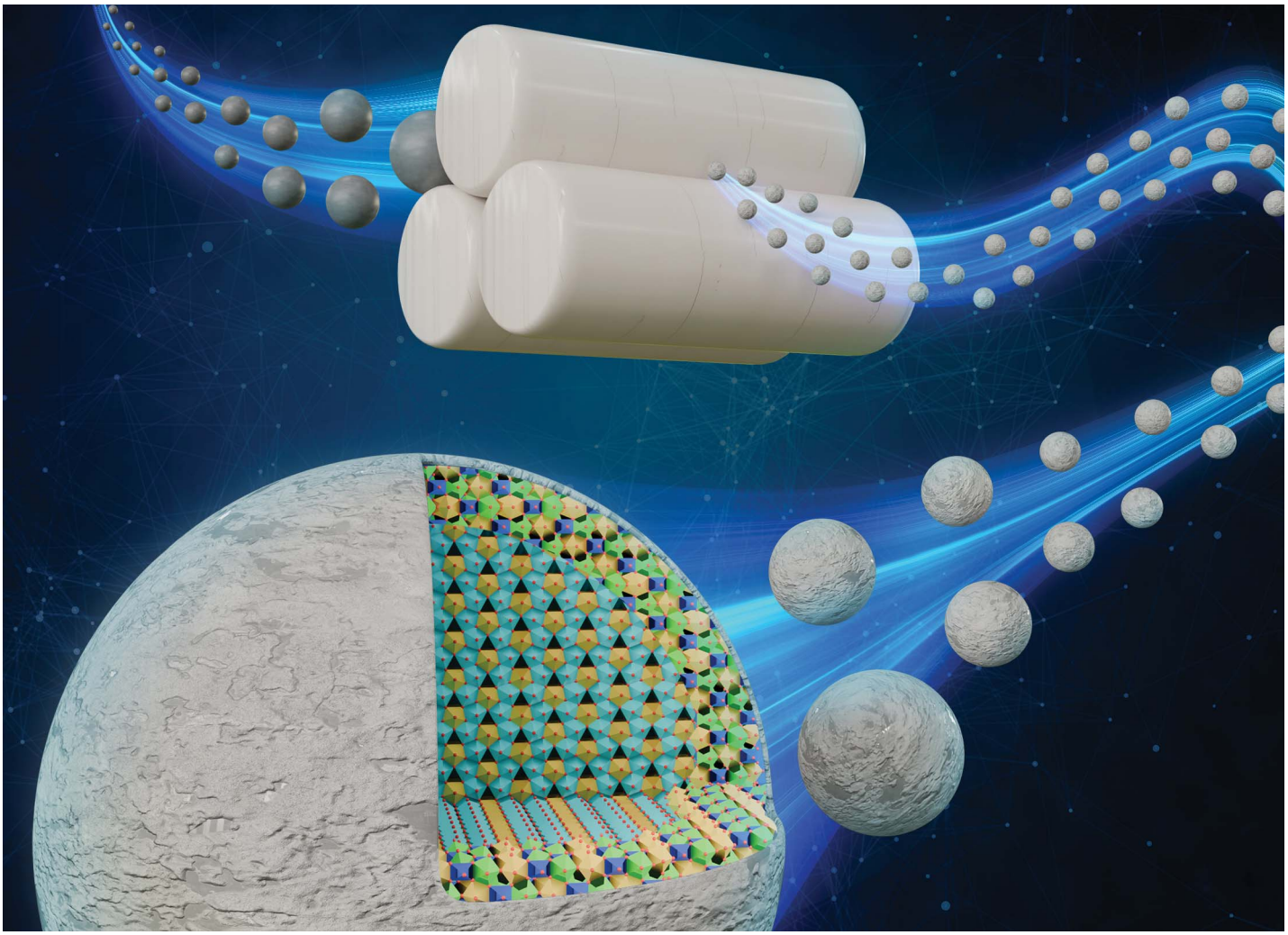

Showcasing research from the Materials and Chemistry Group, Nuclear Nonproliferation Division, Oak Ridge National Laboratory, Tennessee, USA.

Mechanochemical α to β phase transition of U_3O_8

This work examines the kinetics and mechanism of the mechanochemical α- to β-U_3O_8 phase transition, improving our understanding of the thermodynamic relationship between the two polymorphs. Milling of α-U_3O_8 using different milling media shows an ingrowth of the β-phase over time, with observed correlation between media density, percent conversion and lattice strain. Anisotropic peak broadening within collected X-ray diffraction powder patterns suggests preservation of uranium polyhedral layered sheets. Preservation of these sheets implies a shear-induced slip mechanism occurring through in-plane shifting of uranium polyhedra along lattice planes perpendicular to the polyhedral sheets.

Image reproduced by permission of Jordan M. Roach *et al.*, *RSC Mechanochem.*, 2026, **3**, 56.

As featured in:

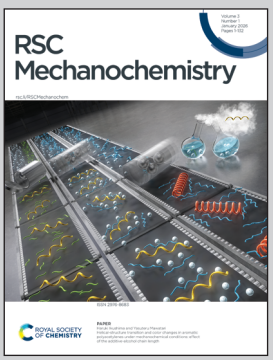

See Jordan M. Roach *et al.*, *RSC Mechanochem.*, 2026, **3**, 56.

ROYAL SOCIETY OF CHEMISTRY

rsc.li/RSCMechanochem

Registered charity number: 207890

RSC Mechanochemistry

ROYAL SOCIETY OF CHEMISTRY

PAPER

View Article Online
View Journal | View Issue

Cite this: *RSC Mechanochem.*, 2026, **3**, 56

Mechanochemical α to β phase transition of U_3O_8

Jordan M. Roach, * Tyler L. Spano and Andrew Miskowiec

Received 8th April 2025
Accepted 24th November 2025

DOI: 10.1039/d5mr00046g

rsc.li/RSCMechanochem

Recognized as the most stable phase of uranium oxide, α-U_3O_8 is widely used throughout the nuclear fuel cycle for safe storage and transportation. There is, however, a lack of understanding of the thermodynamic relationship between α-U_3O_8 and its polymorph, β-U_3O_8. This research contributes new knowledge regarding the kinetics and mechanism of a previously described mechanochemical phase transition between the α- and β-U_3O_8 polymorphs to improve the understanding of their thermodynamic relationship. In this work, tumble milling of α-U_3O_8 using different milling media shows an ingrowth of the β-phase over time, with an observed correlation between media density, percent conversion and lattice strain. Anisotropic peak broadening observed within collected X-ray diffraction powder patterns suggests the preservation of uranium polyhedral layered sheets throughout the milling process. Preservation of the sheets implies a shear-induced slip mechanism occurring through in-plane shifting of uranium polyhedra along lattice planes perpendicular to the polyhedral sheets.

1. Introduction

The most stable oxide phase of uranium, α-U_3O_8, is formed upon heating of most uranium materials in air.[1–3] For this reason, α-U_3O_8 has a significant presence within the nuclear fuel cycle for storage and transportation purposes as well as a source material. However, although α-U_3O_8 is common, questions still exist on the thermodynamic and mechanistic relationship between its formation and that of its polymorph, β-U_3O_8. Though also kinetically stable under ambient conditions, the β-phase is reported to be produced directly from α-U_3O_8 only, and reverts to the α-phase upon heating at temperatures as low as 130 °C.[4] The first method for the consistent synthesis of β-U_3O_8 was published by Karkhanavala and George.[5] Initially designated by the authors as a new "δ-U_3O_8" phase, it was later shown by other works to be crystallographically identical to that of orthorhombic (*Cmcm*) β-U_3O_8.[6,7] The extensive heating procedure described by Karkhanavala and George requires sintering of the α-phase at 1350 °C for 15 days, followed by slow cooling at a rate of 100 °C per day.[5] More contemporary work has shown the sintering time can be reduced to 1 day;[8] however, slow cooling at 100 °C per day is still required to obtain β-U_3O_8. Thermodynamically, the importance of slow cooling to the β-U_3O_8 formation mechanism would appear counterintuitive. If the α-phase is the most stable, then such annealing parameters should result in its formation over that of the β-phase. Owing to the high temperature of conversion, *in situ* structural analysis of U_3O_8 *via* powder X-ray diffraction or Raman spectroscopy is challenging; therefore, the exact mechanism for thermal conversion is unknown.

Nuclear Nonproliferation Division, Oak Ridge National Laboratory, Oak Ridge, TN 37831, USA. E-mail: roachjm@ornl.gov

An initial report of a mechanically induced phase transformation from α- to β-U_3O_8 was described by Herak in 1970.[9] The phase transition was observed to occur during pressing of α-U_3O_8 pellets. Repeated cycling of pellet pressing was performed, resulting in the presence of X-ray diffraction peaks of β-U_3O_8 being observed; subsequently, a shear-induced mechanism was proposed. Since Herak's initial report, only a handful of studies have examined mechanochemical effects of U_3O_8, primarily by Kovacheva *et al.*[10–13] These studies aimed to evaluate the effects on α-U_3O_8 within a planetary ball mill under various conditions, of which the primary result is mechanochemical reduction of α-U_3O_8 to UO_2. Similar reductions of α-U_3O_8 using planetary ball mills have been reported by others exploring the mechanical chlorination[14] and sulfurization[15] of uranium oxides. No tangible evidence of β-U_3O_8 is reported within any of the aforementioned studies, and no other mention of similar observations appear within the literature.

In first reporting the Raman and IR spectra of β-U_3O_8, Miskowiec *et al.* described that broad similarities in lattice dynamics can be expected between the α- and β-polymorphs of U_3O_8, owing to significant parallels in the polymorphs' structures.[8] These similarities can be observed briefly by comparison of both structures in Fig. 1. Both structures are composed solely of U–O polyhedral sheets connected through bridging μ_2-oxygen atoms. Whereas α-U_3O_8 consists entirely of pentagonal bipyramids, the β-phase contains both square and pentagonal bipyramids. However, both structures are composed of mixed valent U^{+5}/U^{+6} metallic centers.[16,17] Based on observations by Herak, the structural similarities between U_3O_8 phases may also be extended to their thermodynamic behavior.[9] A phase transition initiated by simple hand grinding or pressing of the material suggests that a low-energy barrier exists between the polymorphs.

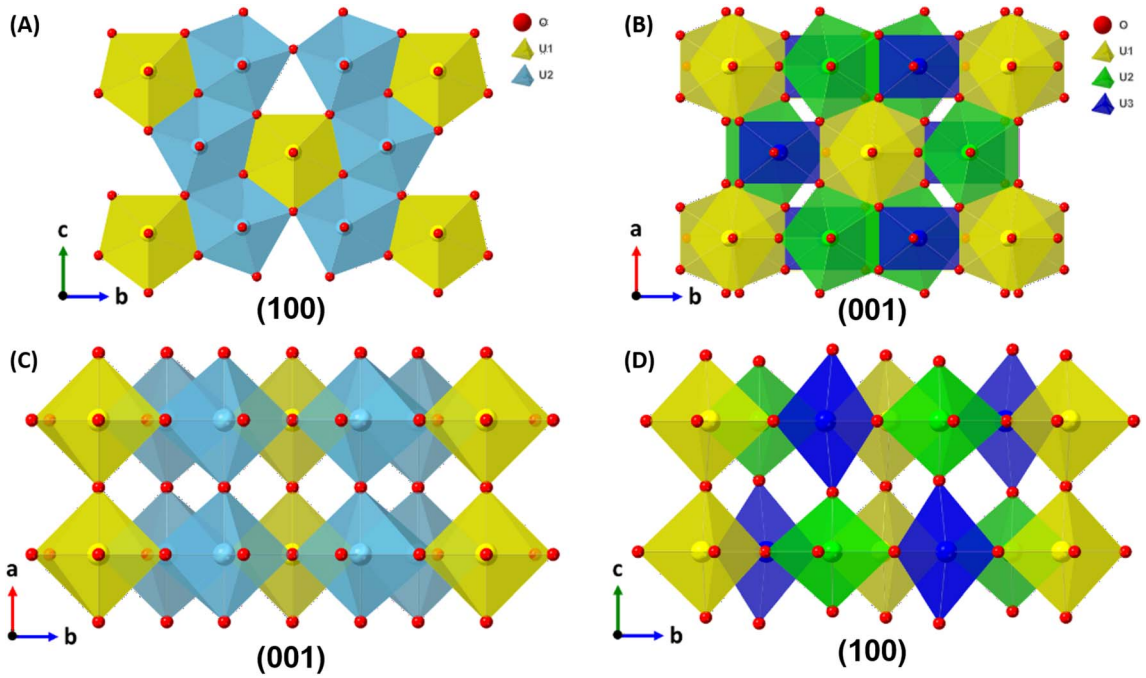

Fig. 1 Crystal structures of α-U_3O_8 (A and C) and β-U_3O_8 (B and D) as determined by Loopstra using neutron diffraction.[18,19]

The current work corroborates the mechanically induced α to β-phase transition first proposed by Herak.[9] Three different milling media materials of varying densities were used to examine their effects on the formation of the β-phase. Characterization of the milled samples show an increase in β-U_3O_8 concentration with increased milling media density and time. Anisotropic peak broadening observed within collected X-ray powder patterns suggests the preservation of uranium polyhedra sheets throughout the milling process. As such, a shear induced slip mechanism that occurs along lattice planes perpendicular to the polyhedra sheets is proposed.

2. Materials and methods

Bulk α-U_3O_8 was produced from uranyl nitrate hexahydrate [$UO_2(NO_3)_2 \cdot 6H_2O$] by initial drying overnight at 100 °C, followed by calcination at 750 °C for 4 h. Resulting material was characterized using powder X-ray diffraction (PXRD). Milling of α-U_3O_8 samples was carried out using a XRD-Mill McCrone (Retsch) with agate, zirconia, and corundum grinding media. Each trial used a 125 mL (45 mm × 84 mm) polypropylene jar with 48 cylindrical grinding elements (13 mm × 13 mm). Per milling trial, 3 g of α-U_3O_8 was loaded into the milling jar with the chosen grinding media. Short-term milling trials had samples milled from 15 to 75 min in 15 min increments, whereas long-term trials had material milled from 2 to 10 h in 2 h increments. Milling was performed at a speed of 1167 rpm. Effects of a higher milling speed were examined using agate milling media set to 1500 rpm. All material was removed from the milling jar between time increments and thoroughly mixed to allow for uniform sampling.

Samples of milled U_3O_8 were analyzed using PXRD. Sample powders were mixed gently by hand with NIST SRM 640e (Si line position standard) and placed on a zero-background silicon plate. Powder patterns were collected *via* a Proto Mfg. AXRD benchtop X-ray diffractometer using a Dectris area detector. Data were collected using a Cu K_α source (λ = 1.541 Å) with a collection range of 15°–75° 2θ with 0.02° steps and 20 s dwell time. Powder patterns in their entirety for all three milling systems can be found in the SI (Fig. S1–S3). Whereas data were collected between 15° and 75° 2θ, the range of the powder patterns was restricted to the 23°–30° 2θ for ease of analysis. This was done due to the low intensity of the most prominent β-U_3O_8 peak relative to the α peaks. Background was subtracted using asymmetric least squares smoothing. Due to the significant overlap of diffraction peaks between the α and β-phases, and significant lower peak intensities coupled with peak broadening, direct quantification of the β-phase was made impractical. Since direct measurement of β-phase in-growth was difficult, conversion of α-U_3O_8 to the β-phase was calculated by taking the quotient of experimental peak amplitudes for the (031) diffraction peak of the α-phase to theoretically calculated peak amplitudes of the β-phase. All PXRD figures show data normalized to the (031) peak of α-U_3O_8 with slight smoothing using two-point adjacent averaging. Additional characterization of select PXRD patterns was performed using the Williamson–Hall method to extract crystallite size and strain values using select α-U_3O_8 diffraction peaks spanning the range of the collected data.

Scanning electron microscopy (SEM) samples were prepared *via* suspension of sample material in ethanol, followed by drop casting onto carbon tape affixed to aluminum stubs. Imaging was performed using a Zeiss Gemini 460 electron microscope, and subsequent image capture was performed using ATLAS control software (Zeiss). Images were collected at a working

distance of 8.5 mm with a probe current and voltage of 195 pA and 20 kV, respectively.

Raman spectra of select milled samples were analyzed using a Renishaw inVia micro-Raman spectrometer equipped with 785 nm (300 μW) and 532 nm (30 μW) excitation lasers coupled with 1200 l mm^{-1} and 2400 l mm^{-1} gratings respectively and a 20× lens objective. Individual spectra were collected at four random points per sample with each spectrum consisting of 15 accumulations, 20s each. Due to low intensity using the 532 nm wavelength, the sample milled for 600 min with zirconia media required 30 accumulations for reasonable interpretation. Individual spectra for each sample were averaged, smoothed using 5 point adjacent averaging and normalized with OriginPro software.

3. Results and discussion

3.1. Milling speed

Initial trials examined the effects of milling speed on the formation of β-U_3O_8. Using agate milling media, samples of α-U_3O_8 were milled at medium (1167 rpm) and high (1500 rpm) speeds from 15 to 75 min. Fig. 2A and B show the resulting PXRD patterns for the medium and high-speed milling products, respectively. Use of a medium milling speed shows a gradual increase in the β-phase peak at 25.1° 2θ from 15 to 75 min. This gradual increase is in contrast to the high speed milling system in which a large increase in the β-phase is observed initially at 15 min, after which peak intensity appears to gradually decrease with extended milling time. A noticeable amount of peak broadening is observed within the high-speed system but is not seen within the medium-speed system. This broadening is associated with higher energy grinding that occurs because of increased rotation speeds.

Intensities of the (200) β-U_3O_8 diffraction peak for both milling speeds are plotted in Fig. 2C. The resulting plots confirm the qualitative observations from the powder patterns. At a medium milling speed, no β-phase is detected until 30 min (about 2.4 a.u.), after which a gradual constant increase to about 3.6 a.u. at 75 min is observed. When milled at the highest speed, a large increase of the β-phase initially occurs, reaching 5.5 a.u. However, continued milling results in a constant decrease of the β-phase, reaching 1.1 a.u. at 75 min. The cause of the decrease in the relative percentage of the β-phase may be attributed to two possibilities. The first relates to a two-step process in which initial high energy input results in a kinetically favorable crystal phase change from α to β; however, continued energy input leads to a thermodynamically favorable mechanism where the system relaxes back to the α-phase. The second possibility for the decrease in relative percentage is attributed to peak broadening. As milling time increases and grinding of the sample powder is extended, material is ground to significantly finer particle sizes, leading to peak broadening. Owing to the low intensity of the β-phase diffraction peaks relative to the α-phase, minor broadening within the system may significantly affect the quantifiability of the β-phase diffraction peaks. This effect will be examined further in Section 3.2. Based on the results from varying the milling speed, continued examination of the milling process was performed with the use of the medium milling speed.

3.2. Milling media

To examine the effects of different milling media on the α- to β-U_3O_8 phase transition, three different milling media—agate, corundum, and zirconia—were examined. Milling media were chosen based on material density, which has been shown to be a parameter affecting milling products.[20–22] The respective PXRD patterns from the resulting samples are shown in Fig. 3. Extended milling times within the agate system (Fig. 3A) beyond 75 min show little to no observable changes to overall β-peak intensity or shape. However, minor broadening is seen within the α peak, which would suggest similar effects may be occurring within the β-phase. Broadening of diffraction peaks is noticeably increased with the use of corundum (Fig. 3B). As milling time increases within the corundum system, the β peak also appears to increase significantly when compared with the agate system. However, owing to the close proximity of the α- and β-peaks, potential exists for broadening effects to impact overall peak height. Similarly, significant broadening is observed within the zirconia system (Fig. 3C). Extended milling of sample powders using the zirconia milling media results in extensive peak broadening and a decrease in overall diffraction

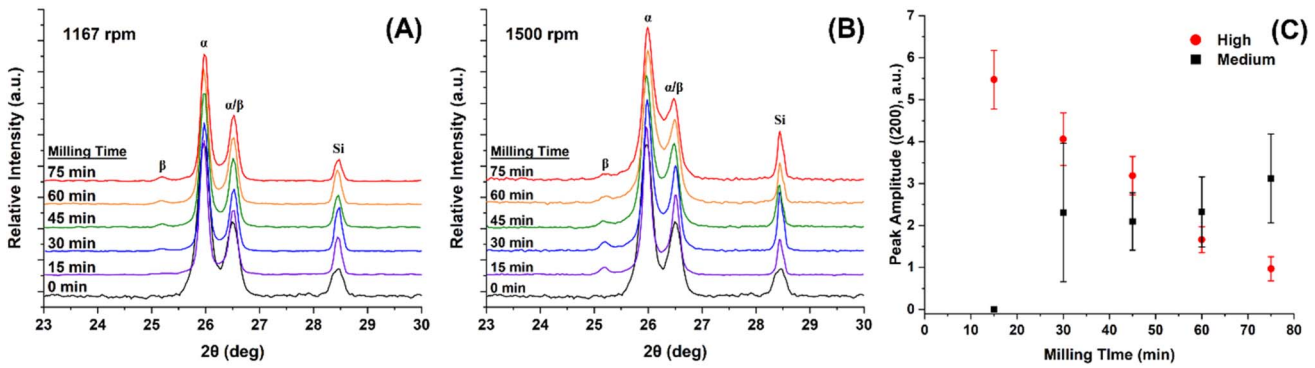

Fig. 2 PXRD patterns for U_3O_8 samples milled with agate media at 1167 (A) and 1500 (B) rpm. Peak amplitudes of the (200) β-U_3O_8 diffraction peak (25.1° 2θ) at high and medium milling speeds with increasing milling time (C).

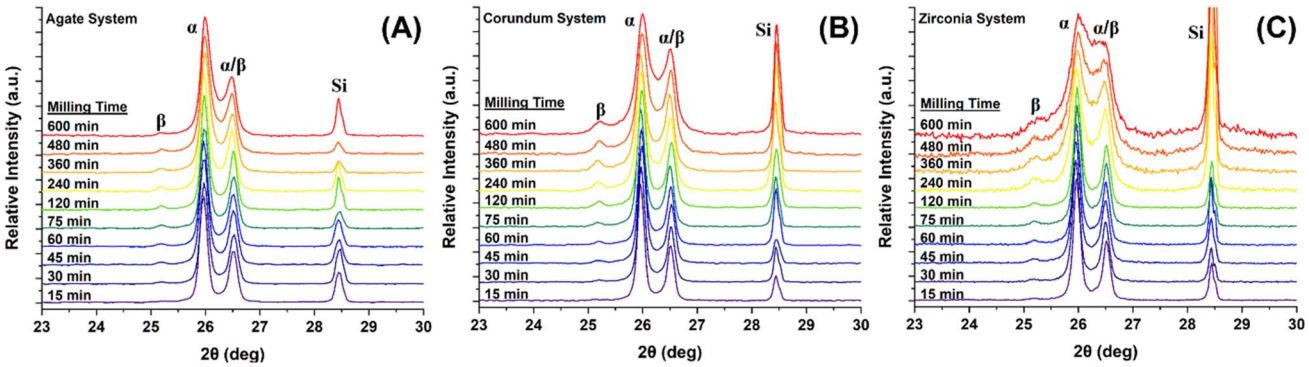

Fig. 3 PXRD patterns for U_3O_8 samples milled with agate (A), corundum (B), and zirconia (C) milling media at 1167 rpm.

intensity. Fig. S4 shows X-ray powder patterns for all three systems without normalization to the (031) peak of α-U_3O_8. This side-by-side comparison shows an increase in broadening effects that correlates well with the density of the examined milling media: agate, 2.5–2.7 g mL; corundum, 3.99 g mL; and zirconia, 5.68 g mL^{-1}.[23] As density of the milling media increases, the force exerted on the U_3O_8 during milling is increased. This increased exerted force results in considerably reduced particle sizes, leading to broadening. The results may also correspond to the hardness of the milling media. However, a direct relationship exists between the method of production and the hardness of synthetic materials.[24,25] As such, without experimental values of hardness for the corundum or zirconia media within the current work, such a relationship cannot be made with any certainty.

Fig. 4 shows SEM images of milled samples using each milling media after 30 and 600 min. After 30 min of milling, particles within the agate system appear relatively uniform in size (Fig. 4B). However, a mixed population of particle sizes is present within both the corundum and zirconia systems

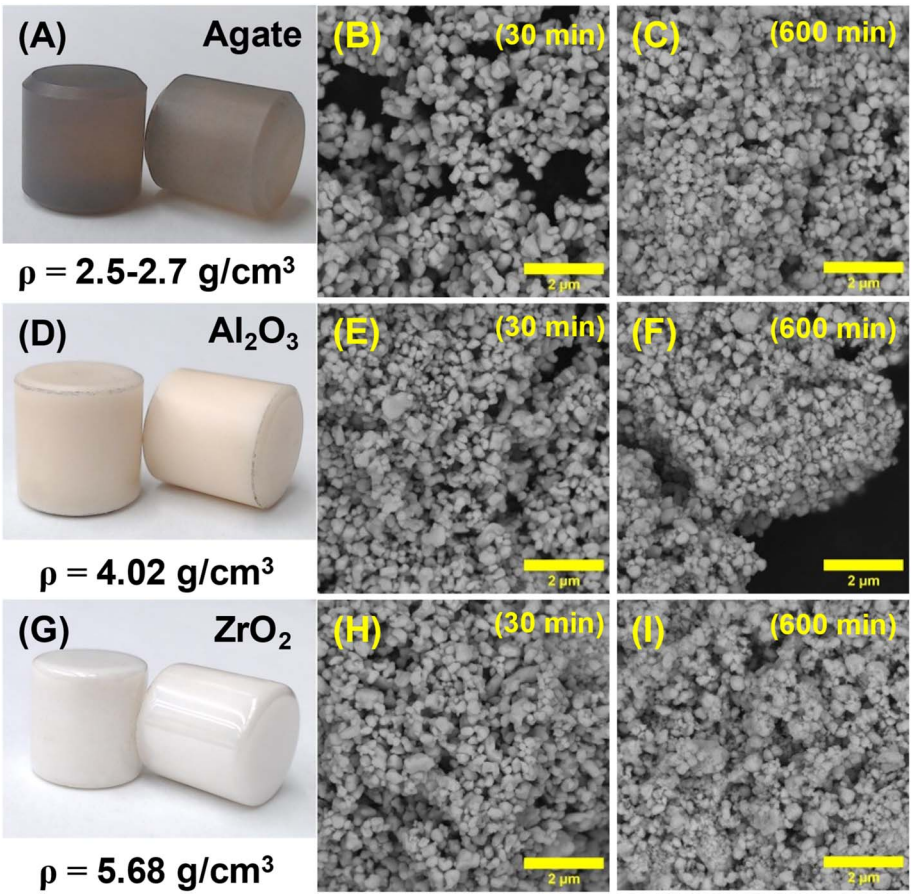

Fig. 4 Agate (A), corundum (D), and zirconia (G) milling media and corresponding SEM images of U_3O_8 powder after milling for 30 min (B, E, and H) and 600 min (C, F, and I).

(Fig. 4E–H). A decrease in particle size becomes more apparent with the extension of milling time to 600 min. The most significant decrease is observed within the zirconia system, in which exceptionally fine particles appear to form agglomerates (Fig. 4I). These images appear to visually agree with the trend observed with peak broadening as a function of both milling time and media. This relationship can be further quantified through calculation of the average crystallite domain size using the Williamson–Hall method.[26–28]

Unlike the traditional Scherrer method which interprets peak broadening solely as a function of crystallite size, use of the Williamson–Hall method allows for dual calculation of both average crystallite size as well as lattice strain.[26–28] This is commonly represented by the linear equation:

$$\beta_{(hkl)}\cos\theta = \frac{K\lambda}{d} + 4\varepsilon\sin\theta \quad (1)$$

where $\beta_{(hkl)}$ is the peak broadening for a given diffraction peak, θ is the peak center, d is the crystallite size and ε is the lattice strain. Plotting of $\beta\cos\theta$ *versus* $4\sin\theta$ allows for determination of both crystallite size and strain through the slope and intercept of the fitted line respectively. Plots created from diffraction data of all three milling media systems after 15, 60 and 600 min are shown in Fig. 5. Subsequent data derived from each plot are presented in Table 1 and confirms the observed decrease in average crystallite size. An increase in strain is also noted to occur with increased milling time. This will be discussed further in Section 3.3.

Because of the low intensity and broadening of the (200) β-U_3O_8 diffraction peak, Rietveld refinement and direct fitting of the diffraction patterns for quantitative analysis are difficult. To best examine the formation of the β-phase within the milling systems, the research team applied an indirect approach through analysis of the (031) peak of α-U_3O_8. This analysis correlates the change in the amplitude (A_{hkl}) of the diffraction peak with time to the amount of material converted to β-U_3O_8. Furthermore, this analysis is completed under the assumptions that within the evaluated system, the only physical changes occurring to the α-phase are conversion to the β-phase and a constant decrease in crystallite size with increasing milling times, as observed in Fig. 5. A more appropriate value for this analysis is the integrated intensity (I_{hkl}) of the given Bragg peak. This value should remain relatively consistent even with significant broadening and, therefore, any changes to it would indicate conversion. However, convolution of lower intensity peaks within the immediate 2θ range of the (031) peak and difficulty in modeling background intensities both result in questionable precision in determining $I_{(031)}$ values using traditional peak fitting. For this reason, evaluating the change in $A_{(031)}$ was determined as the best option within the given system.

As mentioned previously, significant broadening of the diffraction peaks occurs with extended milling times. To evaluate changes in $A_{(031)}$ owing to material conversion, changes due to crystallite size broadening must first be modeled. Theoretical amplitudes (A_{Theor}) for a given diffraction peak were calculated using the height portion of a general gaussian function:

$$A_{\mathrm{Theor}} = \frac{A_0}{w_t\sqrt{2\pi}} \quad (2)$$

where A_0 is the measured amplitude of the diffraction peak at the given starting time, and w_t is the full width at half maximum of the diffraction peaks being evaluated. The resulting values were then normalized to the experimental peak amplitude. Fig. 6 shows the calculated A_{Theor} values plotted alongside

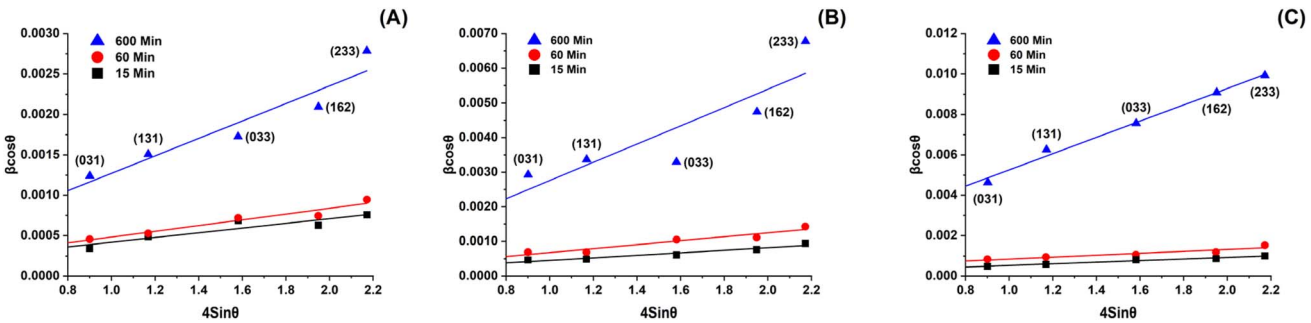

Fig. 5 Williamson–Hall plots created from U_3O_8 diffraction data from agate (A), corundum (B), and zirconia (C) milling media systems after 15, 60 and 600 min of milling.

Table 1 Calculated average crystallite size and lattice strain for milled U_3O_8 samples

	Size (nm)			Strain (10^{-3})		
Milling time (min)	Agate	Corundum	Zirconia	Agate	Corundum	Zirconia
15	1122	1594	1071	0.072	0.091	0.398
60	1166	1245	387	0.089	0.141	0.473
600	756	1178	118	0.270	2.636	4.025

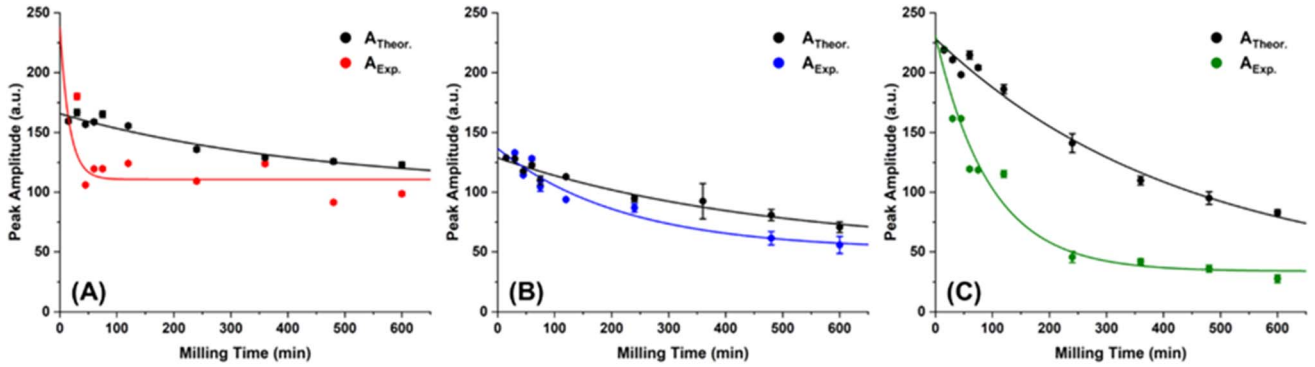

Fig. 6 Calculated $A_{(031)}$ values plotted with experimental values as a function of milling time for agate (A), corundum (B), and zirconia (C) systems.

experimental $A_{(031)}$ values. The experimental value for the corundum system at 360 min of milling was visually determined to be an outlier (Fig. S5) and, therefore, was not included within the analysis. Observation of the plots shows that the experimental amplitudes for the diffraction peaks are noticeably lower than those of the theoretical values. Additionally, the rates at which the experimental values decrease over time appear to be faster than what is predicted to occur from a decrease in crystallite size alone showing conversion of the material.

Taking the quotient of the theoretical and experimental values allows for quantification of the remaining amount of α-U_3O_8 within the system. Fig. 7 shows these values for all three milling systems with calculated best-fit lines showing the systems follow an asymptotic trend. The most prominent result from Fig. 7 is the significant difference in conversion rate of the corundum system *versus* that of either the agate or zirconia systems. Both agate and zirconia systems show a significant amount of conversion within the first 120 min of milling, followed by a conversion plateau, which suggests some type of mechanochemical equilibrium. In comparison, the corundum system shows a much more gradual conversion rate that does not appear to plateau. Such a difference in conversion rate is potentially the result of a physical difference between the milling media, such as the roughness of the milling media itself.

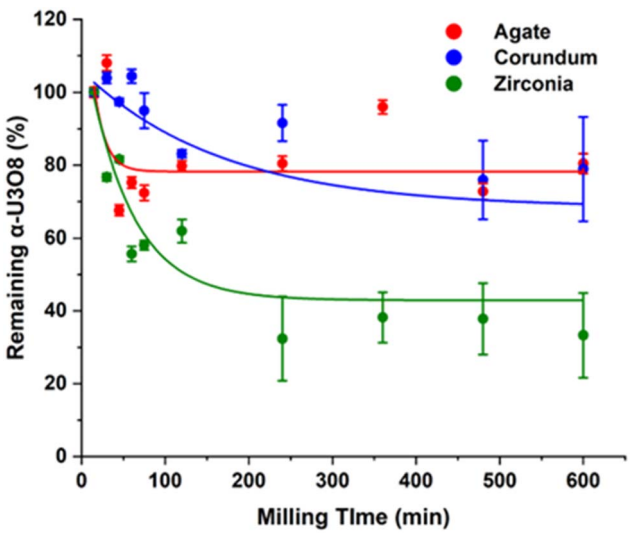

Fig. 7 Calculated percent of remaining α-U_3O_8 with increasing milling time.

Observation of the data also shows that the amount of conversion follows the same pattern relative to milling media density/hardness (agate < corundum < zirconia). However, whereas the agate and corundum systems show modest conversion to the β-phase (*i.e.*, 24.5% and 29.8%, respectively), the zirconia system suggests a noteworthy and significant conversion of 60% at 600 min. The research presents a challenge in confirming either (1) if such a conversion rate is, in fact, occurring or (2) if the limit in which the accuracy of the amplitude-based analysis has more likely been reached. Fig. 6C shows a difference of about 75 a.u. Within $A_{(031)}$ at 120 min and 240 min within the zirconia system; this difference is the largest between two adjacent points for any system. The significant broadening within the PXRD data is observed to begin at this point within Fig. S4. As described earlier, SEM images of the material after 600 min of milling using zirconia media show a large amount of fine particulate. Therefore, this result suggests that within the zirconia system, a size effect is not accounted for within the current method of analysis.

Observation of the current data shows results similar to those originally reported by Herak of a mechanically induced α- to β-U_3O_8 phase transition.[9] Results herein show the amount of β-U_3O_8 produced is affected by milling time, speed, and choice of milling media. Denser and harder milling media appear to increase the amount of the β-phase produced; however, these characteristics also result in a rapid decrease in particle size with extended milling times. The resulting significant decrease in particle size, especially within the zirconia system, at longer milling times makes exact quantification of the β-phase by current means difficult.

3.3. Mechanistic consideration

As discussed in Section 1, Herak proposed that the mechanism for the mechanochemical transition of α-to β-U_3O_8 was induced by shear forces.[9] Herak proposed this mechanism because of the observed transformation occurring after repeated cycling of

cold pellet pressing. In contrast, numerous additional mechanochemical investigations of α-U_3O_8 have shown that rather than a physical conversion of the crystal phase, a chemical reduction from α-U_3O_8 to UO_2 can occur.[10–15] Within the current study, no signs of reduction to UO_2 are observed, suggesting the mechanism for reduction is unique from that of the physical phase transition. Reduction of oxide materials has been addressed elsewhere and is reported to occur owing to a mechanochemical mechanism also observed in transition metal systems.[29–31] The exact mechanism for the reduction process is not described at length by any single publication; however, the presence of impact force is commonly attributed to the process. Note that the studies reporting a reduction to UO_2 use a planetary ball mill configuration (Fig. 8A). Within this style of set-up, milling jars and the supporting disk are rotated in opposing directions, resulting in centrifugal and coriolis forces acting on the milling media.[32] Subsequently, sample material within this configuration is acted on by friction (F_μ), shear (F_τ), and impact (F_I) forces resulting from ball–ball and ball–wall interactions.[33] The types of forces present differ from the tumble-style mill used in the current investigation where a significant impact force is absent. The tumble-style mill uses cylindrical milling media tightly packed within a plastic milling jar (Fig. 8B). Because of the close packing and softer jar composition (as opposed to stainless steel, agate, or zirconia jars within the planetary mill studies), little to no impact forces are present. Rather the system relies primarily on F_μ and F_τ forces to mill the material, resulting in an overall lower-energy system compared with that of a planetary mill.

The effects of using a lower-energy milling system are described by Fuentes and Takacs[33] in their review of preparing multicomponent oxides *via* mechanochemical methods. The authors describe how the hard, brittle nature of oxide particles require a stress threshold to be met before a reaction, such as reduction, can occur. As a result, higher-energy systems (*i.e.*, planetary mills) are required to achieve chemical reactions. Therefore, it can be inferred that the milling system within the current work achieves the activation energy needed to induce physical change within the material (α → β-U_3O_8) but does not exceed the energy threshold required to result in a chemical change (α-U_3O_8 → UO_2). Because no reduction of α-U_3O_8 is observed within the current tumble mill system in the absence of an impact force, such a force can be considered necessary for the reduction to UO_2 to occur. Furthermore, within the current system where the only physical forces present are friction and shear forces and only a crystal phase transition is observed, the shear-induced mechanism proposed by Herak is corroborated.[9] An additional factor to be considered is that of heat. Due to the mechanical forces involved within both systems a portion of the input energy is converted to heat. Both friction and shear forces may produce moderate increases in temperature depending on milling media and jar choice.[34] Due to the current experimental set-up, direct measuring of thermal energy within the system is not obtainable. Therefore, the effects of heat within the milling process cannot be ruled out as being part of a proposed mechanism. These results emphasize the importance of mill choice within the broader realm of mechanochemical investigations. The results also signal a unique opportunity for the investigation of low-energy milling systems to obtain exotic material phases otherwise not easily synthesized *via* traditional thermal treatment.

3.4. U_3O_8 structural implications

The corroboration of a shear-induced phase transition mechanism between α- and β-U_3O_8 advocates for another look at the structural relationship between the two polymorphs. An improved understanding of the mechanism may give enhanced insight into the formation of the β structure and its relationship to the α-polymorph. This section discusses the investigation of the structural relationship of the polymorphs through the frame of the described shear mechanism and proposes a slip mechanism occurring perpendicular to the polyhedral sheets within the α-U_3O_8 structure, resulting in the formation of the β-phase. A general, more in-depth comparative description of both structures has been published previously;[8,19] however, a brief overview is provided here.

Both structures are composed of repeating layers of U–O polyhedra connected through bridging equatorial oxygen atoms, with each polyhedral layer connected *via* interstitial bridging oxygen atoms. Within the α-U_3O_8 structure (Fig. 1A–C), all layers are identical, composed solely of pentagonal bipyramidal polyhedra with two crystallographically unique uranium sites. Bond valence calculations of the individual sites yield valence sums of 5.30 and 5.37 *vu* for U_1 and U_2 sites, respectively. These values had originally been described to suggest either a $U^{5+}{}_2U^{6+}O_8$ or $U^{4+}U^{6+}{}_2O_8$ composition;[35] however, more contemporary works have shown the U^{5+}/U^{6+} composition to be more accurate from density functional theory[17] and supported

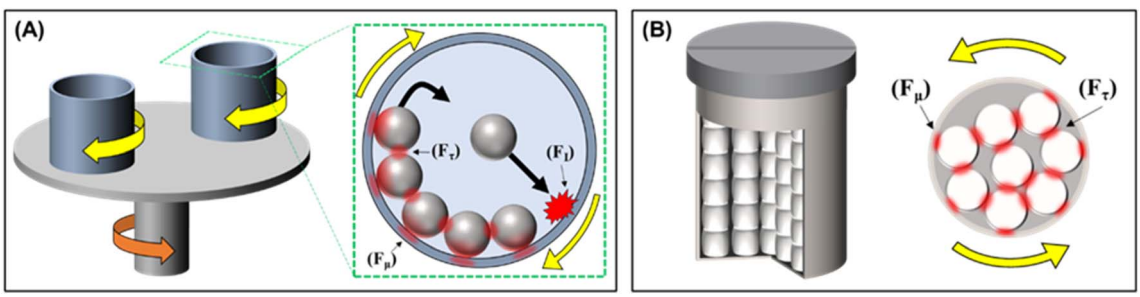

Fig. 8 Schematic of a planetary ball mill (A) and tumble mill (B).

by X-ray absorption near edge spectroscopy.[16] Interstitial bridging oxygen atoms show near-linear bonds connecting sheets of U–O polyhedra, with all exhibiting equidistant bond lengths of 2.07 Å. Though similar in arrangement to that of the α-phase, β-U_3O_8 is composed of two alternating sheets containing two distinct pentagonal and one tetragonal bipyramid with three different U sites (Fig. 1B–D). Bond valence sums for the crystallographically unique sites are $U_1 = 5.27$, $U_2 = 5.96$, and $U_3 = 5.01$ *vu*, giving an oxidation state composition similar to that of the α-phase.

The presence of a tetragonal bipyramid within the β-U_3O_8 structure is of note as it requires breaking an O–U equatorial bond during transformation from the α-phase. The presence of a shear induced slip plane would allow for the shifting of uranium polyhedra and account for breaking of bonds needed to form the β-phase. Shear mechanisms have been observed in another uranium oxide phase transition, β-U_4O_9 → α-U_3O_8, in which shear forces are shown to allow for the relaxation of "crumpled" polyhedral sheets of β-U_4O_9 to the linear polyhedral sheets of α-U_3O_8.[36] However, in the current system, both phases are comprised of flat polyhedral sheets, devoid of the corrugation observed in β-U_4O_9. Fig. S6 shows a side-by-side comparison of a single uranium polyhedral sheet from both the α and β-U_3O_8 phases. From this view it could be inferred that applying a shear force to the α-phase may result in the stretching of the chains of U2 polyhedra resulting in the more linear alternating U1–U2 polyhedral chain within β-U_3O_8. "Straightening" of these chains would come at the expense of breaking the $O3_\alpha$-$U1_\alpha$ bond within the α-phase, shown more clearly in Fig. 9 (addition of "α" and "β" subscripts to atom labels herein represent their relation to either phase of U_3O_8). Bond valence calculations show the $O3_\alpha$ atom retains a bond valence value of 1.95 *vu* when transitioning from a μ_3 to a μ_2 environment upon structural reorganization to the β-phase, suggesting there are significant changes to electron donation by the atom itself. Instead, energetically favorable changes are observed within neighboring $O5_\alpha$ atoms. Within the α structure, the $O5_\alpha$ site is calculated to have a bond valence of 2.25 *vu* suggesting a higher-than-average electron donation to the uranium centers. Upon breaking of the $O3_\alpha$–$U1_\alpha$ bond, the $O5_\alpha$ atom splits into two crystallographically-unique sites within the β-phase, denoted as $O4_\beta$ and $O5_\beta$, with bond valence sums of 2.11 *vu* and 2.07 *vu* respectively. The decrease in these values would suggest a favorable shift towards a closer-to-ideal valency (*i.e.* 2). This shift is partnered with the shortening and subsequent strengthening of the $O4_\alpha$–$U2_\alpha$ bond. The strengthening of this bond is inferred as its length decreases from 2.714 Å in the α-phase to 2.371 Å in the β-phase. As described, the proposed straightening of the polyhedral chains through the breaking of the $O3_\alpha$–$U1_\alpha$ allows for a similar shear induced phase transition as described by Desgranges *et al.*[36] but does not account for the alternating nature of the layered polyhedral sheets of β-U_3O_8. Therefore, the straightening mechanism may represent a portion of the shear induced mechanism but not its entirety, rather the full mechanism requires understanding of how the alternating sheets of the β-phase form.

Theoretical shifting of individual uranium polyhedral sheets was considered *via* a slip mechanism in-plane to the uranium polyhedral sheets; however, this mechanism would result in the additional breaking of the axial oxygen bridges. Such distortion of the bridging oxygen planes is unlikely based on anisotropic peak broadening observed within the powder diffraction patterns. Fig. S7–S9 show Williamson–Hall plots for all three milling media systems after 15, 60, and 600 min. Included within the plots are additional points corresponding to diffraction peaks originating from the (100), (200), and (300) lattice planes. We observe that both the (200) and (300) points are significantly separated from the rest of the data at all milling times, with the separation of the (100) point becoming more prominent after 600 min of milling. The positioning of these points shows that the diffraction peaks from which they originate are less susceptible to broadening. These lattice planes are parallel to the uranium polyhedral sheets and/or are in-plane with bridging oxygens (Fig. S10). Therefore, upon milling of

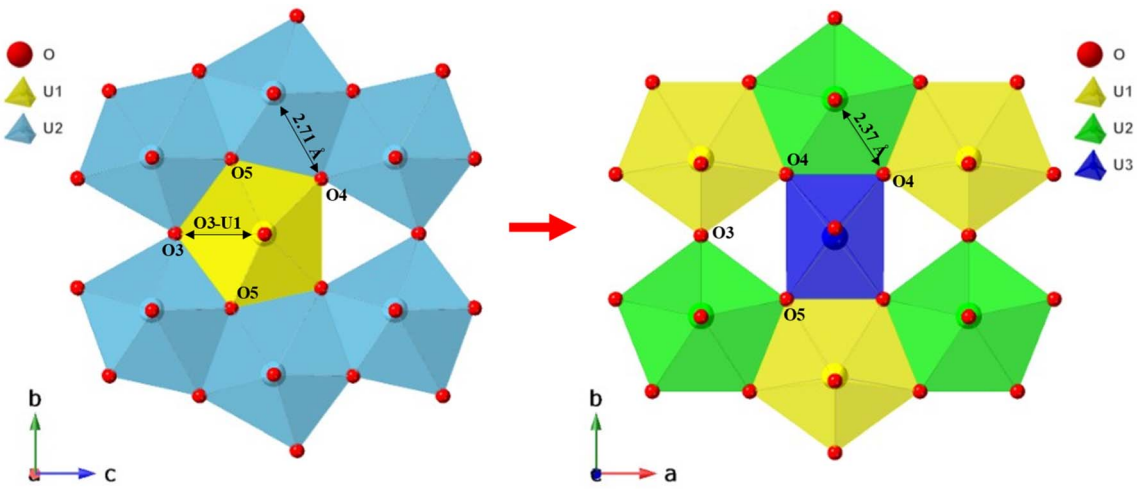

Fig. 9 Isolated clusters of uranium polyhedra from α-U_3O_8 (left) and β-U_3O_8 (right) showing the transition of the hybridized $U1_\alpha$ pentagonal bipyramid to the pentavalent $U3_\beta$ tetragonal bypyrabid.

the material, these lattice planes are preferentially preserved, thus retaining the layered structure. If shifting of the polyhedral sheets parallel to one another were to occur, we would expect the diffraction peak corresponding to the (200) lattice plane containing the axial oxygen bridges to broaden as a result of structural distortion. We therefore speculate that any shear induced slip mechanism is most probable along (001), (010), and (011) planes, perpendicular to the (100) plane. In this way the slip mechanism occurs along the most atom-dense planes with the shortest distance between occupied positions. Additionally, a slip mechanism occurring along planes perpendicular to the uranium polyhedral sheets would account for the alternating nature of individual sheets within the β-U_3O_8 structure as described above. As uranium centers shift along the (100) plane following the slip vector, rearrangement of individual polyhedra allows for shifting of equatorial bonds and subsequent formation of the tetragonal bipyramid within the β-phase. As observed in Table 1, an increase in milling time results in a significant increase in lattice strain, by a factor of ten in the case of the zirconia system. As strain forces increase, partial alleviation of the applied forces may come at the expense of such a slip plane.

It is possible that this proposed mechanism is more likely to occur along particle edges and surfaces where initial defects and those introduced from milling are more apparent and the relative shear force is strongest.[37,38] This would agree well with the observation of limited conversion to the β-phase. Additionally, as the bulk material continues to decrease in average particle size with increased milling, the conversion to the β-phase may increase as surface and edge characteristics surpass that of the bulk. A common characteristic of nanostructured oxides processed through mechanochemical methods exhibit a "core–shell" configuration.[39] Within such a configuration a well-ordered inner core (the bulk) is surrounded by a layer of disordered interfaces and surface structures. In addition to the continued decrease in size, the additional loss of long-range order in the outer shell results in significant loss of diffraction pattern resolution. This significant loss in diffraction pattern resolution would align well with the observation of a decrease in β-phase peak intensity at higher milling speeds as discussed in Section 3.1. To further probe the formation of the β-phase, select samples of milled material were evaluated using Raman spectroscopy.

A common method for the characterization of uranium materials, Raman spectroscopy is a surface-sensitive method capable of probing local chemical environments, *e.g.* coordination and bonding. Samples were evaluated using both 785 nm and 532 nm excitation lasers. Differences in photon wavelength can affect the overall penetration depth of the analysis method and theoretically aid in observing a stronger presence of the β-phase at the surface of particles.[40] However, due to the size of the particles themselves (about 0.1 μm to 1.5 μm), both excitation wavelengths would likely penetrate beyond a single particle layer and therefore make distinction of the position of the β-phase (surface *vs.* bulk) unlikely. Fig. S11 shows Raman spectra of samples milled for 15 and 600 min from all three milling media systems. Evaluation of spectra from samples within the agate system (Fig. S11A and B) show no significant spectral changes between the two milling times with use of either excitation wavelength. However, changes are observed within spectra from both the corundum (Fig. S11C and D) and zirconia (Fig S11E and F) systems. Within both systems the ingrowth of peaks at 183, 264 and 516 cm^{-1} align well with reported Raman peak positions of β-U_3O_8.[8] It is of note that the peak at 183 cm^{-1} is not observed within spectra collected using the 785 nm laser. It is also observed that the other two β-phase peaks are less apparent within these spectra. This difference is attributed to the use of the 785 nm excitation wavelength itself which though commonly used, has been shown to result in weaker peak intensities when analyzing α-U_3O_8.[41] However, both excitation lasers do show an increase of intensity within the 425–500 nm range that would again align with potential β-U_3O_8 at 455 and 470 cm^{-1}.[8] An overall change in background intensity between the 15 min and 600 min samples is also observed with the baseline intensities increasing following the trend of agate < corundum < zirconia. This trend mirrors that which was discussed in Section 3.2 regarding the difference in overall forces produced from the milling media based on differences in density/hardness. Though Raman spectroscopic analysis is not capable of providing additional insight into the mechanisms of the mechanochemical α → β-U_3O_8 phase transition, the overall presence of the β-phase within the Raman spectra is more easily observed than the low intensity peaks within PXRD. Therefore, it may be beneficial for future investigations into the mechanism to focus on spectroscopic studies where both intensity and resolution of phase-specific peaks may be improved.

4. Conclusions

This work provides an in-depth investigation into the mechanochemical phase transition of α-to β-U_3O_8 and corroborates the shear-induced mechanism originally proposed by Herak in 1970.[9] The use of different milling media shows that increasing media density results in an increase to lattice strain within the milled material which correlates to an increased formation of the β-phase. Anisotropic peak broadening observed within collected X-ray diffraction powder patterns suggests the preservation of uranium polyhedral layered sheets throughout the milling process. Preservation of the parallel uranium sheet structure and bridging axial oxygen bridges would imply a shear-induced slip mechanism that occurs with in-plane shifting of uranium polyhedra along lattice planes perpendicular to the polyhedral sheets. It is speculated that the amount of β-phase may continue to increase with milling time as particle size decreases and surface/edge defect concentrations increase. The potential for the proposed mechanism to initiate from surface and/or edge defects has potential implications for understanding the thermal synthesis of β-U_3O_8. One may consider the initial nucleation of the β-phase at higher temperatures followed by expansive growth with slow cooling. Additional investigations are required for further support of the current purposed mechanism, as well as its implications for a defect-initiated nucleation mechanism at elevated

temperatures. However, the current work continues to bridge the gap in knowledge that exists between common α-U_3O_8 and its more elusive β-phase polymorph.

Conflicts of interest

There are no conflicts to declare.

Data availability

The data supporting this article have been included as part of the supplementary information (SI). Supplementary information is available. See DOI: https://doi.org/10.1039/d5mr00046g.

Acknowledgements

This manuscript has been authored by UT-Battelle, LLC, under contract DE-AC05-00OR22725 with the US Department of Energy (DOE). The US government retains and the publisher, by accepting the article for publication, acknowledges that the US government retains a nonexclusive, paid-up, irrevocable, worldwide license to publish or reproduce the published form of this manuscript, or allow others to do so, for US government purposes. DOE will provide public access to these results of federally sponsored research in accordance with the DOE Public Access Plan (https://www.energy.gov/doe-public-access-plan). This work was supported by the National Nuclear Security Administration.

References

1 N. Raje, S. Manna, D. K. Ghonge, S. B. Roy and A. V. R. Reddy, Impurity characterization and thermal decomposition mechanism of ammonium diuranate during in-situ synthesis of U_3O_8 using simultaneous TG-DTA-FTIR and PXRD measurements, *J. Anal. Appl. Pyrolysis*, 2014, **109**, 21–28, DOI: 10.1016/j.jaap.2014.07.017.

2 M. Assulin, R. Yam, A. Kossoy, E. Elish and A. Shemesh, Equilibrium Fractionation of Oxygen Isotopes in the U_3O_8–Atmospheric Oxygen System, *ACS Omega*, 2022, **7**(50), 47040–47047, DOI: 10.1021/acsomega.2c06148.

3 J. I. Ranasinghe, L. Malakkal, E. Jossou, B. Szpunar and J. A. Szpunar, Comprehensive study on the electronic and optical properties of α-U_3O_8, *Comput. Mater. Sci.*, 2020, **171**, 109264, DOI: 10.1016/j.commatsci.2019.109264.

4 K. J. Notz, C. W. Huntington and W. Burkhardt, Hydrogen Reduction of Uranium Oxides. A Phase Study by Means of a Controlled-Atmosphere Diffractometer Hot Stage, *Ind. Eng. Chem. Process Des. Dev.*, 1962, **1**(3), 213–217, DOI: 10.1021/i260003a010.

5 M. D. Karkhanavala and A. M. George, δ-U_3O_8, A high temperature modification: Part I: preparation and characterization, *J. Nucl. Mater.*, 1966, **19**(3), 267–273, DOI: 10.1016/0022-3115(66)90149-8.

6 B. O. Loopstra, On the existence of δ-U_3O_8; a comment on papers by Karkhanavalla and George, and by Amirthalingam, *J. Nucl. Mater.*, 1969, **29**(3), 354–355, DOI: 10.1016/0022-3115(69)90214-1.

7 R. Herak and B. Jovanović, On the existence of δ-U_3O_8, *Inorg. Nucl. Chem. Lett.*, 1969, **5**(8), 693–697, DOI: 10.1016/0020-1650(69)80168-6.

8 A. Miskowiec, T. Spano, R. Hunt and J. M. Kurley, Optical vibrational spectra of β-U_3O_8, *J. Nucl. Mater.*, 2022, **568**, 153894, DOI: 10.1016/j.jnucmat.2022.153894.

9 R. Herak, A stress induced α-U_3O_8-β-U_3O_8 transformation, *J. Inorg. Nucl. Chem.*, 1970, **32**(12), 3793–3797, DOI: 10.1016/0022-1902(70)80553-X.

10 P. Kovacheva, G. Avdeev and D. Todorovsky, Mechanochemically induced synthesis of UO_{2+x} and uranium–thorium mixed oxides from sol–gel produced precursors, *J. Radioanal. Nucl. Chem.*, 2011, **287**(2), 519–524, DOI: 10.1007/s10967-010-0707-1.

11 P. Kovacheva, D. Todorovsky and D. Radev, Mechanochemistry of the 5f-elements compounds. 5. Influence of the reaction medium on the mechanochemically induced reduction of U_3O_8, *J. Radioanal. Nucl. Chem.*, 2011, **287**(1), 193–197, DOI: 10.1007/s10967-010-0666-6.

12 P. Kovacheva, N. Minkova, D. Todorovsky and D. Radev, Mechanochemistry of the 5f-element compounds, *J. Radioanal. Nucl. Chem.*, 2007, **274**(3), 465–471, DOI: 10.1007/s10967-006-6925-x.

13 P. Kovacheva, D. Todorovsky, D. Radev, V. Mavrudiev, R. Petrov, D. Kovacheva and K. Petrov, Mechanochemical effects in U_3O_8, *J. Radioanal. Nucl. Chem.*, 2005, **262**(3), 573–578, DOI: 10.1007/s10967-005-0478-2.

14 S. Kitawaki, T. Nagai and N. Sato, Chlorination of uranium oxides with CCl_4 using a mechanochemical method, *J. Nucl. Mater.*, 2013, **439**(1), 212–216, DOI: 10.1016/j.jnucmat.2013.03.017.

15 N. Sato and A. Kirishima, Application of Sulfide Process to Fuel Debris Treatment, *Energy Procedia*, 2013, **39**, 102–109, DOI: 10.1016/j.egypro.2013.07.196.

16 G. Leinders, R. Bes, J. Pakarinen, K. Kvashnina and M. Verwerft, Evolution of the Uranium Chemical State in Mixed-Valence Oxides, *Inorg. Chem.*, 2017, **56**(12), 6784–6787, DOI: 10.1021/acs.inorgchem.7b01001.

17 N. A. Brincat, S. C. Parker, M. Molinari, G. C. Allen and M. T. Storr, Density functional theory investigation of the layered uranium oxides U_3O_8 and U_2O_5, *Dalton Trans.*, 2015, **44**(6), 2613–2622, DOI: 10.1039/C4DT02493A.

18 B. Loopstra, Neutron diffraction investigation of U_3O_8, *Acta Crystallogr.*, 1964, **17**(6), 651–654, DOI: 10.1107/S0365110X6400158X.

19 B. Loopstra, The structure of β-U_3O_8, *Acta Crystallogr., Sect. B*, 1970, **26**(5), 656–657, DOI: 10.1107/S0567740870002935.

20 A. Krusenbaum, S. Grätz, G. T. Tigineh, L. Borchardt and J. G. Kim, The mechanochemical synthesis of polymers, *Chem. Soc. Rev.*, 2022, **51**(7), 2873–2905, DOI: 10.1039/D1CS01093J.

21 G. Mucsi, A review on mechanical activation and mechanical alloying in stirred media mill, *Chem. Eng. Res. Des.*, 2019, **148**, 460–474, DOI: 10.1016/j.cherd.2019.06.029.

22 S. Palaniandy and N. H. Jamil, Influence of milling conditions on the mechanochemical synthesis of $CaTiO_3$ nanoparticles, *J. Alloys Compd.*, 2009, **476**(1), 894–902, DOI: 10.1016/j.jallcom.2008.09.133.

23 *CRC Handbook of Chemistry and Physics*, ed. J. R. Rumble, CRC Press/Taylor & Francis, Boca Raton, FL, 106th edn (Internet Version 2025), 2023.

24 R. W. Rice, C. C. Wu and F. Boichelt, Hardness–Grain-Size Relations in Ceramics, *J. Am. Ceram. Soc.*, 1994, **77**(10), 2539–2553, DOI: 10.1111/j.1151-2916.1994.tb04641.x.

25 T. P. Hoepfner and E. D. Case, The influence of the microstructure on the hardness of sintered hydroxyapatite, *Ceram. Int.*, 2003, **29**(6), 699–706, DOI: 10.1016/S0272-8842(02)00220-1.

26 A. Khorsand Zak, W. H. Abd Majid, M. E. Abrishami and R. Yousefi, X-ray analysis of ZnO nanoparticles by Williamson–Hall and size-strain plot methods, *Solid State Sci.*, 2011, **13**(1), 251–256, DOI: 10.1016/j.solidstatesciences.2010.11.024.

27 S. A. Hassanzadeh-Tabrizi, Precise calculation of crystallite size of nanomaterials: a review, *J. Alloys Compd.*, 2023, **968**, DOI: 10.1016/j.jallcom.2023.171914.

28 S. Dutta, S. Chattopadhyay, A. Sarkar, M. Chakrabarti, D. Sanyal and D. Jana, Role of defects in tailoring structural, electrical and optical properties of ZnO, *Prog. Mater. Sci.*, 2009, **54**(1), 89–136, DOI: 10.1016/j.pmatsci.2008.07.002.

29 J. Xie, K. Huang, Z. Nie, W. Yuan, X. Wang, Q. Song, X. Zhang, C. Zhang, J. Wang and J. C. Crittenden, An effective process for the recovery of valuable metals from cathode material of lithium-ion batteries by mechanochemical reduction, *Resour., Conserv. Recycl.*, 2021, **168**, 105261, DOI: 10.1016/j.resconrec.2020.105261.

30 V. Šepelák, M. Menzel, K. D. Becker and F. Krumeich, Mechanochemical Reduction of Magnesium Ferrite, *J. Phys. Chem. B.*, 2002, **106**(26), 6672–6678, DOI: 10.1021/jp020270z.

31 J. Che, W. Zhang, L. Xia, J. Chen, P. Wen, B. Ma and C. Wang, A Facile and Environmentally Friendly Approach for Lead Recovery from Lead Sulfate Residue *via* Mechanochemical Reduction: Phase Transformation and Reaction Mechanism, *ACS Sustain. Chem. Eng.*, 2021, **9**(30), 10227–10239, DOI: 10.1021/acssuschemeng.1c02587.

32 H. X. Khoa, S. Bae, S. Bae, B.-w. Kim and J. S. Kim, Planetary Ball Mill Process in Aspect of Milling Energy, *J Powder Mater.*, 2014, **21**(2), 155–164, DOI: 10.4150/KPMI.2014.21.2.155.

33 A. F. Fuentes and L. Takacs, Preparation of multicomponent oxides by mechanochemical methods, *J. Mater. Sci.*, 2013, **48**(2), 598–611, DOI: 10.1007/s10853-012-6909-x.

34 K. Uzarevic, N. Ferdelji, T. Mrla, P. A. Julien, B. Halasz, T. Friscic and I. Halasz, Enthalpy *vs.* friction: heat flow modelling of unexpected temperature profiles in mechanochemistry of metal–organic frameworks, *Chem. Sci.*, 2018, **9**(9), 2525–2532, DOI: 10.1039/c7sc05312f.

35 P. C. Burns, R. C. Ewing and F. C. Hawthorne, The crystal chemistry of hexavalent uranium; polyhedron geometries, bond-valence parameters, and polymerization of polyhedra, *Canad. Mineral.*, 1997, **35**(6), 1551–1570.

36 L. Desgranges, G. Baldinozzi, D. Simeone and H. E. Fischer, Refinement of the α-U_4O_9 crystalline structure: new insight into the $U_4O_9 \rightarrow U_3O_8$ transformation, *Inorg. Chem.*, 2011, **50**(13), 6146–6151, DOI: 10.1021/ic200316b.

37 S. Mateti, M. Mathesh, Z. Liu, T. Tao, T. Ramireddy, A. M. Glushenkov, W. Yang and Y. I. Chen, Mechanochemistry: a force in disguise and conditional effects towards chemical reactions, *Chem. Commun.*, 2021, **57**(9), 1080–1092, DOI: 10.1039/d0cc06581a.

38 N. K. Yu, L. F. Rasteiro, V. S. Nguyen, K. M. Golabek, C. Sievers and A. J. Medford, Evaluating the Role of Metastable Surfaces in Mechanochemical Reduction of Molybdenum Oxide, *JACS Au*, 2025, **5**(1), 82–90, DOI: 10.1021/jacsau.4c00758.

39 V. Sepelak, A. Duvel, M. Wilkening, K. D. Becker and P. Heitjans, Mechanochemical reactions and syntheses of oxides, *Chem. Soc. Rev.*, 2013, **42**(18), 7507–7520, DOI: 10.1039/c2cs35462d.

40 M. Hardy and H. O. M. Chu, Laser wavelength selection in Raman spectroscopy, *Analyst*, 2025, **150**, 1986, DOI: 10.1039/d5an00324e.

41 S. Karcher, R. Mohun, T. Olds, M. Weber, K. Kriegsman, X. Zhao, X. Guo, C. Corkhill, D. Field and J. McCloy, Benefits of using multiple Raman laser wavelengths for characterizing defects in a UO_2 matrix, *J. Raman Spectrosc.*, 2022, **53**, 988–1002, DOI: 10.1002/jrs.6321.